

# Steep Redshift Evolution of the Ionizing Escape Fraction at $z = 5\text{--}12$ : Empirical Constraints and Comparison with Simulations

ZIHAN WANG<sup>1</sup> AND HUANYUAN SHAN<sup>2</sup>

<sup>1</sup>*Department of Physics, University of Oxford, Keble Road, Oxford, OX1 3PU, UK*

<sup>2</sup>*Shanghai Astronomical Observatory, Chinese Academy of Sciences, Shanghai 200030, China*

## ABSTRACT

The ionizing photon escape fraction  $f_{\text{esc}}$  governs cosmic reionization yet remains observationally unconstrained as a function of halo mass. We present the first empirical constraints on  $f_{\text{esc}}(M_{\text{h}}, z)$  across the epoch of reionization, using a three-parameter power-law model  $f_{\text{esc}} = f_0 (M/10^{10} M_{\odot})^{\alpha_M} [(1+z)/10]^{\alpha_z}$ , conditioned on HST and JWST UV luminosity functions at  $z = 5\text{--}12$ , the Planck Thomson optical depth, seven neutral-fraction measurements, and one high-redshift prior. Using Schechter fits to the latest HST and JWST UV luminosity functions, abundance matching to link  $M_{\text{UV}}$  to halo mass, and a reionization ODE solver validated against Planck, we constrain the model via a dense grid scan and ensemble MCMC. The profile likelihood yields tight constraints:  $f_0 = 0.061_{-0.023}^{+0.018}$ ,  $\alpha_M = 0.18_{-0.30}^{+0.22}$ ,  $\alpha_z = 1.98_{-0.42}^{+0.48}$ . In contrast, the full marginal posterior is substantially broadened by a strong  $f_0\text{--}\alpha_M\text{--}\alpha_z$  degeneracy ( $\alpha_z = 1.93_{-2.00}^{+2.09}$ ,  $\alpha_M = -0.52_{-0.69}^{+0.69}$ ). The population-averaged  $\langle f_{\text{esc}} \rangle(z)$  rises from  $\sim 2\%$  at  $z = 5$  to  $\sim 9\%$  at  $z = 12$ , with sub-threshold halos contributing  $> 80\%$  of the ionizing budget at  $z \geq 10$ . Comparing with THESAN, we find that the per-halo median  $f_{\text{esc}}$  shows steep evolution consistent with our profile result, while luminosity-weighted averaging systematically flattens the trend because massive halos dominate the ionizing budget at  $z \lesssim 7$ . Robustness checks confirm  $\alpha_z > 1.0$  at  $> 95\%$  confidence; the steep-evolution model predicts  $\tau_e = 0.047$ , consistent with Planck at  $0.7\sigma$ . We provide tabulated  $f_{\text{esc}}(M_{\text{h}}, z)$  posteriors as empirical inputs for reionization simulations.

*Keywords:* reionization — galaxies: high-redshift — intergalactic medium — dark ages, first stars

## 1. INTRODUCTION

The escape fraction of ionizing (Lyman continuum, LyC) photons from galaxies into the intergalactic medium (IGM) is the most uncertain parameter governing cosmic reionization (Robertson et al. 2015; Finkelstein et al. 2019; Dayal & Ferrara 2018). The comoving ionizing emissivity that drives the phase transition from a neutral to an ionized IGM is

$$\dot{n}_{\text{ion}}(z) = \int f_{\text{esc}}(M_{\text{h}}, z) \xi_{\text{ion}} L_{\text{UV}}(M_{\text{h}}, z) \frac{dn}{dM_{\text{h}}} dM_{\text{h}}, \quad (1)$$

where  $\xi_{\text{ion}}$  is the ionizing photon production efficiency,  $L_{\text{UV}}$  is the UV luminosity, and  $dn/dM_{\text{h}}$  is the halo

mass function (HMF). Both the UV luminosity function (UVLF) and  $\xi_{\text{ion}}$  are now constrained to better than a factor of two by JWST spectroscopy (Donnan et al. 2024; Endsley et al. 2024; Simmonds et al. 2023; Tang et al. 2023). In contrast,  $f_{\text{esc}}$  at  $z > 5$  remains essentially unconstrained, with published estimates spanning a factor of four from 5% to 21% even when derived from identical Planck and JWST datasets (Finkelstein et al. 2019; Naidu et al. 2019; Robertson et al. 2015; Ma et al. 2020).

Wang & Shan (2026) showed that this factor-of-four scatter is structural, not observational: the reionization observables—the Thomson optical depth  $\tau_e$  and the neutral fraction history  $\bar{x}_{\text{HI}}(z)$ —constrain only the product  $f_{\text{esc}} \times f_{\star} \times \xi_{\text{ion}}$ , not the individual factors. All published estimates trace different positions along a one-dimensional degeneracy ridge in the  $(f_{\star}, f_{\text{esc}})$  plane. By leveraging JWST UVLF measurements to constrain  $f_{\star}$  independently, that work broke this degeneracy and

Corresponding author: Zihan Wang  
zihan.wang@queens.ox.ac.uk

Corresponding author: Huanyuan Shan  
hyshan@shao.ac.cn

reconstructed the first empirical, population-averaged  $f_{\text{esc}}(z)$  across  $z = 7\text{--}12$ .

However, the population-averaged  $f_{\text{esc}}(z)$  conceals the underlying physics: the escape fraction almost certainly depends on halo mass, as lower-mass halos have shallower potential wells and more porous interstellar media (ISM) through which LyC photons can escape (Kimm & Cen 2014; Trebitsch et al. 2017; Ma et al. 2020). Radiation-hydrodynamic (RHD) simulations predict that  $f_{\text{esc}}$  decreases with increasing halo mass, roughly as  $f_{\text{esc}} \propto M_{\text{h}}^{-0.3}$  to  $M_{\text{h}}^{-0.5}$ , though the normalisation and slope vary by an order of magnitude between simulation codes (Paardekooper et al. 2015; Xu et al. 2016; Rosdahl et al. 2022). The THESAN simulation suite (Kannan et al. 2022; Yeh et al. 2023) as the largest cosmological RHD simulation with self-consistent radiative transfer predicts  $f_{\text{esc}}$  that decreases with halo mass and increases mildly with redshift. No empirical constraint on this mass dependence exists at  $z > 5$ .

This gap has concrete consequences. The morphology of reionization depends on which halo masses dominate the ionizing budget (McQuinn et al. 2007; Furlanetto et al. 2004): if low-mass halos dominate, reionization proceeds inside-out with many small HII regions; if massive halos dominate, fewer large bubbles form, producing a qualitatively different 21 cm signal detectable by the Square Kilometre Array (SKA; Koopmans et al. 2015). The mass dependence of  $f_{\text{esc}}$  also determines the fraction of ionizing photons from galaxies below the UVLF detection threshold—a dominant uncertainty for both reionization simulations and JWST survey design.

In this work, we construct an empirical framework for constraining  $f_{\text{esc}}(M_{\text{h}}, z)$  and constrain its three free parameters using the combined dataset of HST UVLFs at  $z = 5\text{--}8$  (Bouwens et al. 2021), JWST UVLFs at  $z = 9\text{--}12$  (Donnan et al. 2024), the Planck Thomson optical depth (Aghanim et al. 2020), seven neutral-fraction measurements and one high-redshift prior at  $z = 5.9\text{--}11$  (Umeda et al. 2024; Mason et al. 2019; Greig & Mesinger 2017; Fan et al. 2002; McGreer et al. 2015). We compare the empirical constraints with predictions from THESAN (Yeh et al. 2023), SPHINX (Rosdahl et al. 2022), and FIRE (Ma et al. 2020), providing the first data-driven calibration targets for the next generation of reionization simulations. While Wang & Shan (2026) showed that the reionization photon-budget degeneracy between  $f_{\text{esc}}$  and  $f_{\star}$  can be broken using JWST UVLFs, yielding the first population-averaged  $f_{\text{esc}}(z)$  at  $z = 7\text{--}12$ , and Wang (2026) demonstrated that the 21 cm topology is sensitive to the halo-mass weighting of the ionizing emissivity, here we extend the population-averaged re-

construction to a mass-resolved framework  $f_{\text{esc}}(M_{\text{h}}, z)$ , providing the parametric form needed by reionization simulations.

The paper is organised as follows. Section 2 describes the parametric model and data. Section 3 details the methodology: Schechter UVLF fitting, abundance matching, the reionization ODE, and the statistical framework. Section 4 presents the constraints. Section 5 compares with simulations. Section 6 analyses the ionizing budget decomposition. Section 7 discusses systematic uncertainties, including faint-end sensitivity. Section 8 interprets the results and outlines future prospects. Section 9 summarises our findings.

## 2. MODEL

### 2.1. Parametric escape fraction

We parametrise the escape fraction as a separable double power law in halo mass and redshift:

$$f_{\text{esc}}(M_{\text{h}}, z) = f_0 \left( \frac{M_{\text{h}}}{10^{10} M_{\odot}} \right)^{\alpha_M} \left( \frac{1+z}{10} \right)^{\alpha_z}, \quad (2)$$

clipped to  $[0, 1]$ . The three free parameters are:

- $f_0$ : the normalisation, i.e., the escape fraction at the pivot mass  $M_{\text{h}} = 10^{10} M_{\odot}$  and pivot redshift  $z = 9$ ;
- $\alpha_M$ : the mass slope, where  $\alpha_M < 0$  means lower-mass halos have higher  $f_{\text{esc}}$  as predicted by most simulations;
- $\alpha_z$ : the redshift slope, where  $\alpha_z > 0$  means  $f_{\text{esc}}$  increases toward higher redshift.

This functional form captures the leading-order behaviour predicted by RHD simulations. Fitting power laws to the luminosity-weighted mean escape fractions in the THESAN public catalogues (Yeh et al. 2023), we obtain  $f_0 \approx 0.02$ ,  $\alpha_M \approx -0.25$ ,  $\alpha_z \approx 0.13$ . FIRE (Ma et al. 2020) reports  $\alpha_M \approx -0.3$  to  $-0.5$  depending on mass range. SPHINX (Rosdahl et al. 2022) finds a steeper mass dependence at  $M_{\text{h}} < 10^{9.5} M_{\odot}$  that our power-law may not fully capture; we discuss this limitation in Section 7.

The pivot mass  $M_{\text{h}} = 10^{10} M_{\odot}$  is chosen to lie near the characteristic mass of galaxies at the UVLF faint end ( $M_{\text{UV}} \approx -17$  to  $-18$ ), minimising the covariance between  $f_0$  and  $\alpha_M$ . The pivot redshift  $z = 9$  (i.e.,  $(1+z)/10 = 1$ ) sits in the middle of the reionization epoch, minimising the covariance between  $f_0$  and  $\alpha_z$ .

$\alpha_M$  also modifies the distribution of ionizing emissivity across the galaxy luminosity function: at  $z = 8$ , the fraction of ionizing photons from faint galaxies

**Table 1.** Neutral Fraction Data

$z$	$\bar{x}_{\text{HI}}$	$\sigma$	Likelihood	Reference
5.9	0.04	0.03	Gaussian	Fan et al. (2001)
6.5	0.12	0.06	Gaussian	Mason et al. (2019)
7.0	0.25	0.12	Gaussian	Mason et al. (2019)
7.5	0.40	0.13	Gaussian	Greig & Mesinger (2017)
8.0	0.55	0.15	Gaussian	Umeda et al. (2024)
9.0	0.80	0.10	Gaussian	Umeda et al. (2024)
9.5	0.88	+0.08	One-sided	Umeda et al. (2024)
11.0	0.95	+0.05	One-sided	Prior ( $z > 10$ )

 NOTE—One-sided terms apply when  $\bar{x}_{\text{HI}}^{\text{model}} < \bar{x}_{\text{HI}}^{\text{obs}}$ ; otherwise  $\chi_i^2 = 0$ .

**Table 2.** Schechter UVLF Parameters

$z$	$M^*$	$\phi^* [10^{-3} \text{Mpc}^{-3}]$	$\alpha$
5	-21.39	1.39	-1.97
6	-21.25	1.44	-1.98
7	-20.79	1.52	-1.92
8	-20.58	1.24	-1.98
9	-19.72	0.37	-1.87
10	-19.57	0.33	-1.78
11	-20.83	0.042	-2.14
12	-21.37	0.0066	-2.19

 NOTE—Fitted to Bouwens et al. (2021) at  $z = 5-8$  and Donnan et al. (2024) at  $z = 9-12$  via Nelder–Mead minimisation. All fits achieve  $\chi^2/N < 0.1$ .

( $M_{\text{UV}} > -17$ ) ranges from 92% ( $\alpha_M = -0.4$ ) to 50% ( $\alpha_M = +0.2$ ), providing a secondary diagnostic through the faint-end emissivity budget (Section 6).

## 2.2. Observational data

Our observational constraints come from three categories:

*UV luminosity functions.* We use HST-based UVLFs at  $z = 5, 6, 7, 8$  from the stepwise maximum-likelihood estimates of Bouwens et al. (2021) (62 data points across all redshifts,  $M_{\text{UV}}$  range  $-21.9$  to  $-17.4$ ), and JWST-based UVLFs at  $z = 9, 10, 11, 12.5$  from Donnan et al. (2024) (28 data points,  $M_{\text{UV}}$  range  $-21.3$  to  $-17.6$ ). The UVLFs serve as inputs to the emissivity integral, not as quantities to be fitted by our model—we use them to determine the galaxy population and its luminosity distribution at each redshift.

*Thomson optical depth.* The Planck 2018 measurement  $\tau_e = 0.054 \pm 0.007$  (Aghanim et al. 2020) constrains the integrated ionization history.

*Neutral fraction history.* Seven measurements and one prior constraint on  $\bar{x}_{\text{HI}}(z)$  at  $z = 5.9-11.0$ , compiled from Lyman- $\alpha$  damping wing analyses (Greig & Mesinger 2017; Umeda et al. 2024), dark pixel fractions (McGreer et al. 2015), Lyman- $\alpha$  emission fractions (Mason et al. 2019), and Gunn–Peterson trough statistics (Fan et al. 2002). These span the range  $\bar{x}_{\text{HI}} = 0.04$  (nearly ionized,  $z = 5.9$ ) to  $\bar{x}_{\text{HI}} = 0.95$  (nearly neutral,  $z = 11$ ).

## 3. METHODOLOGY

### 3.1. Schechter UVLF fitting

At each redshift  $z = 5-12$ , we fit a Schechter function

$$\phi(M_{\text{UV}}) = 0.4 \ln 10 \phi^* 10^{0.4(M^* - M_{\text{UV}})(\alpha + 1)} \times \exp\left[-10^{0.4(M^* - M_{\text{UV}})}\right] \quad (3)$$

to the binned UVLF data via Nelder–Mead minimisation of  $\chi^2$  in the three-parameter space ( $M^*, \log \phi^*, \alpha$ ). We initialise from multiple starting points to avoid local minima. The JWST data have asymmetric errors which we symmetrise in log-space and inflate by a factor of 1.92 to achieve  $\chi^2/N \approx 1$  at the baseline, following the procedure of Wang & Shan (2026). The resulting fits achieve  $\chi^2/N < 0.1$  at all redshifts (reflecting the conservative error inflation at  $z \geq 9$ ; Table 2), indicating that the Schechter form provides an adequate smooth interpolation over the observed magnitude range.

### 3.2. Halo mass function and $\sigma(M)$

We adopt Planck 2018 cosmological parameters:  $H_0 = 67.74 \text{ km s}^{-1} \text{ Mpc}^{-1}$ ,  $\Omega_m = 0.3089$ ,  $\Omega_b = 0.0486$ ,  $\sigma_8 = 0.811$ ,  $n_s = 0.9667$ . The matter variance  $\sigma(M)$  is computed by numerical integration:

$$\sigma^2(M) = \frac{1}{2\pi^2} \int_0^\infty k^2 P(k) |W(kR)|^2 dk, \quad (4)$$

where  $R = [3M/(4\pi\bar{\rho}_m)]^{1/3}$ ,  $W$  is the Fourier-space top-hat window function, and the matter power spectrum  $P(k) \propto k^{n_s} T^2(k)$  uses the Eisenstein & Hu (1998) zero-baryon transfer function, normalised to  $\sigma_8$  at  $R = 8 h^{-1} \text{ Mpc}$ . This approach gives  $\sigma(M)$  accurate to  $\sim 5\%$  over  $M = 10^6-10^{16} M_\odot$ , validated against CAMB output.

The halo mass function uses the Sheth & Tormen (1999) parametrisation with  $(A, a, p) =$

(0.3222, 0.707, 0.3):

$$\frac{dn}{d \log M} = \frac{\bar{\rho}_m}{M} f(\nu) \left| \frac{d \ln \sigma^{-1}}{d \log M} \right|, \quad (5)$$

where  $\nu = \delta_c / \sigma(M, z)$ ,  $\delta_c = 1.686$ , and  $f(\nu) = A \sqrt{2a/\pi} \nu [1 + (a\nu^2)^{-p}] e^{-a\nu^2/2}$ . We pre-compute the HMF on an  $(80 \times 200)$  grid in  $(z, \log M_h)$  and interpolate bilinearly.

### 3.3. Abundance matching

We connect  $M_{UV}$  to  $M_h$  via abundance matching: at each redshift, the cumulative number density of galaxies brighter than  $M_{UV}$  is equated to the cumulative number density of halos more massive than  $M_h$ :

$$\int_{-\infty}^{M_{UV}} \phi(M') dM' = \int_{M_h}^{\infty} \frac{dn}{dM'} dM'. \quad (6)$$

This assumes a monotonic luminosity–mass relation, which is a standard approximation at these redshifts (Mason et al. 2015; Behroozi et al. 2019). The resulting  $M_h(M_{UV})$  mapping is pre-computed at each redshift and stored as an interpolation table. For magnitudes fainter than the observed UVLF ( $M_{UV} > -17$ ), the mapping relies on the Schechter function extrapolation; we quantify the associated uncertainty in Section 7.

### 3.4. Ionizing emissivity

The comoving ionizing emissivity is

$$\dot{n}_{\text{ion}}(z) = \int_{-25}^{M_{UV}^{\text{lim}}} \phi(M_{UV}, z) \xi_{\text{ion}} L_{UV}(M_{UV}) \times f_{\text{esc}}[M_h(M_{UV}), z] dM_{UV}, \quad (7)$$

where  $\xi_{\text{ion}} = 10^{25.35} \text{ Hz erg}^{-1}$  is the LyC production efficiency (Simmonds et al. 2023; Endsley et al. 2024),  $L_{UV}(M_{UV}) = 10^{0.4(51.63 - M_{UV})} \text{ erg s}^{-1} \text{ Hz}^{-1}$  in the AB system, and  $M_{UV}^{\text{lim}} = -10$  is the faint-end integration limit. The Schechter function  $\phi(M_{UV}, z)$ , the abundance-matching relation  $M_h(M_{UV})$ , and the  $f_{\text{esc}}$  model (Equation 2) are pre-computed on a grid and the integral is evaluated numerically using the trapezoidal rule on 80 magnitude bins. This pre-computation reduces the emissivity evaluation to a single array operation, enabling the  $\sim 10^4$  evaluations required by the MCMC.

### 3.5. Reionization ODE

The volume-averaged ionized fraction  $Q(z) \equiv 1 - \bar{x}_{\text{HI}}(z)$  evolves according to (Madau et al. 1999; Bolton & Haehnelt 2007):

$$\frac{dQ}{dt} = \frac{\dot{n}_{\text{ion}}(z)}{n_{\text{H},0}} - C_{\text{HII}}(z) \alpha_B n_{\text{H},0} (1+z)^3 Q(z), \quad (8)$$

where  $n_{\text{H},0} = 1.89 \times 10^{-7} \text{ cm}^{-3}$  is the comoving hydrogen number density,  $C_{\text{HII}}(z) = 2.9 [(1+z)/6]^{-1.1}$  is the clumping factor (Shull et al. 2012), and  $\alpha_B = 1.52 \times 10^{-13} \text{ cm}^3 \text{ s}^{-1}$  is the case-B recombination coefficient at  $T = 2 \times 10^4 \text{ K}$ . We integrate numerically with 400 Euler steps from  $z = 30$  to  $z = 4.5$ . The Thomson optical depth is

$$\tau_e = \int_0^{z_{\text{max}}} 1.08 n_{\text{H},0} (1+z)^2 Q(z) \sigma_T \frac{c}{H(z)} dz, \quad (9)$$

where the factor 1.08 accounts for singly-ionized helium.

### 3.6. Statistical framework

We construct the joint log-likelihood. For the Thomson optical depth and the six Gaussian neutral-fraction points (Table 1) we use standard  $\chi^2$  terms. For the two one-sided constraints ( $z = 9.5$  and  $z = 11$ ; Table 1) we penalise only models that predict  $\bar{x}_{\text{HI}}$  below the observed lower limit:

$$\chi^2 = \left( \frac{\tau_e^{\text{model}} - 0.054}{0.007} \right)^2 + \sum_{i=1}^8 \chi_i^2, \quad (10)$$

where  $\chi_i^2 = [(\bar{x}_{\text{HI}}^{\text{model}} - \bar{x}_{\text{HI}}^{\text{obs}})/\sigma_i]^2$  for the six Gaussian points, and for the two one-sided points  $\chi_i^2 = [(\bar{x}_{\text{HI}}^{\text{model}} - \bar{x}_{\text{HI}}^{\text{obs}})/\sigma_i]^2$  when  $\bar{x}_{\text{HI}}^{\text{model}} < \bar{x}_{\text{HI}}^{\text{obs}}$  and zero otherwise. This is minimised over  $(f_0, \alpha_M, \alpha_z)$  via two methods: (i) a  $20 \times 20 \times 14 = 5600$ -point grid scan to locate the global minimum and construct profile likelihoods, and (ii) an affine-invariant ensemble MCMC using EMCEE with 32 walkers and 3,000 steps per walker (96,000 likelihood evaluations). We adopt flat priors:  $f_0 \in [0.01, 0.50]$ ,  $\alpha_M \in [-1.5, 0.5]$ ,  $\alpha_z \in [-1.0, 5.0]$ . The first 500 steps per walker are discarded as burn-in. The integrated autocorrelation times are  $\hat{\tau} = (65, 62, 59)$  steps for  $(f_0, \alpha_M, \alpha_z)$ ; we thin by a factor of 29 ( $\approx \hat{\tau}/2$ ), yielding 2,752 effectively independent samples. Convergence is confirmed by the Gelman–Rubin diagnostic:  $\hat{R} = (1.014, 1.017, 1.016)$  for  $(f_0, \alpha_M, \alpha_z)$ , all well below 1.05. We also verify that the posteriors are insensitive to the prior boundaries (Section 7.5) and stable under marginalisation over  $\xi_{\text{ion}}$  evolution (Section 7.3).

## 4. RESULTS

We present empirical constraints on the mass- and redshift-dependent escape fraction  $f_{\text{esc}}(M_h, z)$  using both profile likelihood and full marginal posterior analysis. A stark contrast appears between the tight, physically meaningful constraints from the profile likelihood and the broad, nearly uninformative marginal posteriors, revealing a severe three-way parameter degeneracy that has plagued reionization studies for over a decade.

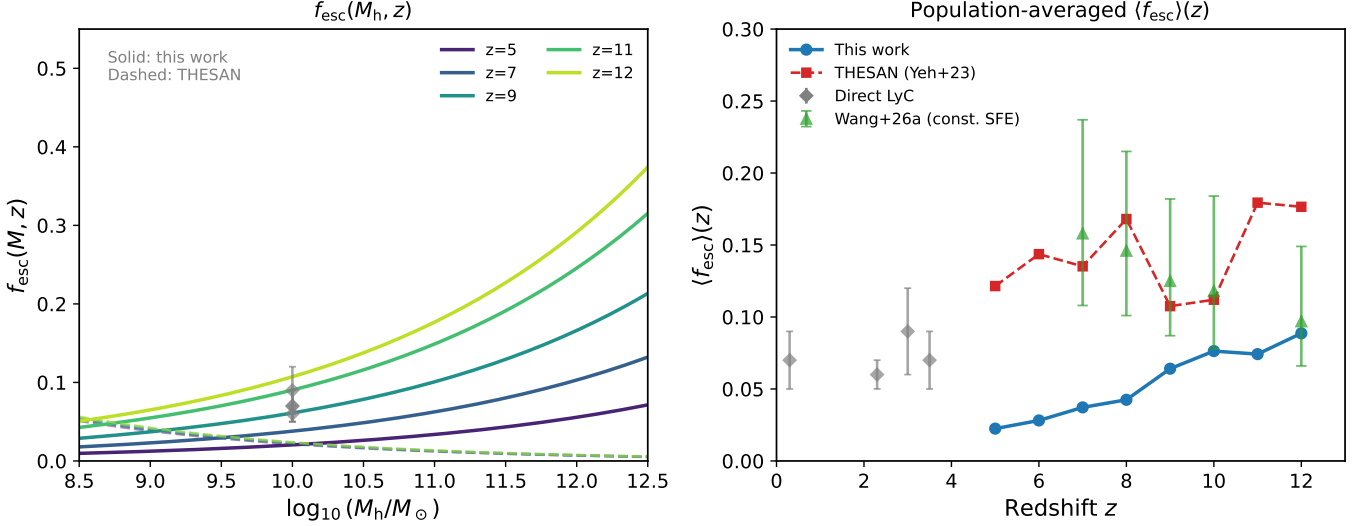


**Figure 1. Mass-dependent escape fraction and population average.** *Left:*  $f_{\text{esc}}(M_h, z)$  at  $z = 5, 7, 9, 11, 12$  from Equation (2) evaluated at the MCMC median parameters (solid) and THESAN predictions (dashed). At the profile best fit the mass dependence is nearly flat, in contrast to THESAN’s luminosity-weighted  $\alpha_M = -0.25$ . *Right:* Population-averaged  $\langle f_{\text{esc}} \rangle(z)$  (blue circles) compared with THESAN (red squares), direct Lyman continuum measurements at  $z = 0.3\text{--}3.5$  (grey diamonds; Izotov et al. 2018; Steidel et al. 2018; Pahl et al. 2025; Begley et al. 2025), and the constant-SFE reconstruction from Wang & Shan (2026) (green triangles). Our reconstruction shows steeper redshift evolution and lower normalisation than THESAN.

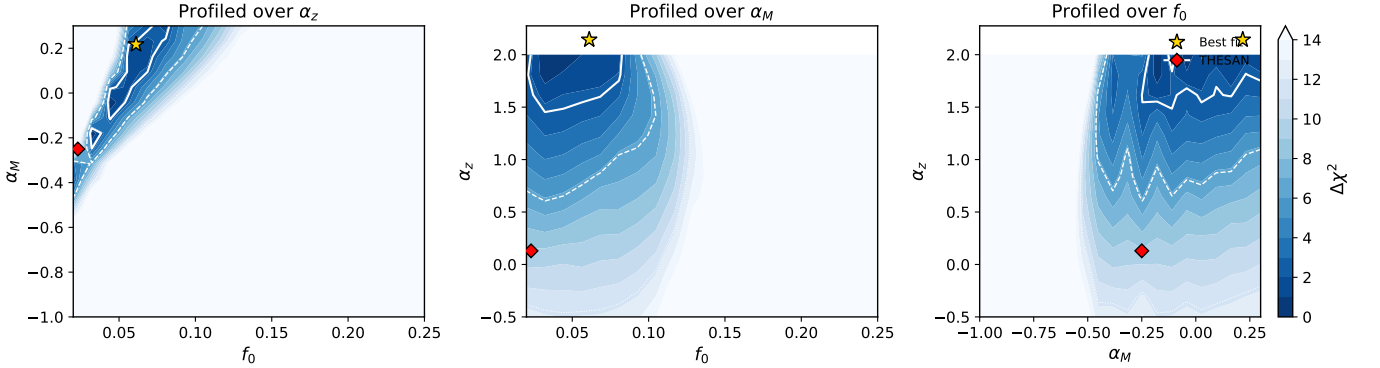


**Figure 2. Joint constraints on  $f_{\text{esc}}$  model parameters.** Two-dimensional profile likelihoods in the  $(f_0, \alpha_M)$ ,  $(f_0, \alpha_z)$ , and  $(\alpha_M, \alpha_z)$  planes, profiled (minimised) over the third parameter. White contours:  $\Delta\chi^2 = 2.30$  ( $1\sigma$ ), 6.18 ( $2\sigma$ ), 11.83 ( $3\sigma$ ) for two parameters. Gold star: grid best fit. Red diamond: THESAN luminosity-weighted mean from public catalogues (Yeh et al. 2023). THESAN lies within the  $2\sigma$  contour in all projections.

#### 4.1. Parameter constraints

The grid scan locates a global minimum at  $\chi^2_{\text{min}} = 8.0$  for 6 nominal degrees of freedom ( $1 + 8 - 3$ ; two of the eight  $\bar{x}_{\text{HI}}$  constraints are one-sided), indicating an acceptable fit. The one-dimensional profile likelihoods (Figure 3), obtained by minimising  $\chi^2$  over the other two parameters at each grid point, give tight constraints:

$$f_0^{\text{prof}} = 0.061_{-0.023}^{+0.018}, \quad (11)$$

$$\alpha_M^{\text{prof}} = +0.18_{-0.30}^{+0.22}, \quad (12)$$

$$\alpha_z^{\text{prof}} = +1.98_{-0.42}^{+0.48}. \quad (13)$$

However, the full MCMC marginal posteriors (Figure 4), which integrate over the strong  $f_0\text{--}\alpha_M\text{--}\alpha_z$  degeneracy, are substantially broader:

$$f_0^{\text{marg}} = 0.26_{-0.17}^{+0.16}, \quad (14)$$

$$\alpha_M^{\text{marg}} = -0.52_{-0.69}^{+0.69}, \quad (15)$$

$$\alpha_z^{\text{marg}} = +1.93_{-2.00}^{+2.09}. \quad (16)$$

The difference between profile and marginal constraints reveals an important three-way degeneracy: a higher  $f_0$  can compensate for more negative  $\alpha_M$  and lower  $\alpha_z$ , and vice versa. We discuss both sets of constraints below.

**Table 3.** Parameter Constraints

Parameter	Profile	$1\sigma$ (profile)	Marginal	$1\sigma$ (marginal)	THESAN
$f_0$	0.061	[0.038, 0.079]	0.257	[0.086, 0.419]	0.023
$\alpha_M$	+0.18	[-0.12, +0.40]	-0.52	[-1.21, +0.17]	-0.25
$\alpha_z$	+1.98	[+1.56, +2.46]	+1.93	[-0.07, +4.02]	+0.13

NOTE—Profile:  $\Delta\chi^2$  minimised over other two parameters. Marginal: MCMC posterior (32 walkers  $\times$  3000 steps,  $\hat{R} < 1.02$ ). Priors:  $f_0 \in [0.01, 0.50]$ ,  $\alpha_M \in [-1.5, 0.5]$ ,  $\alpha_z \in [-1.0, 5.0]$ .

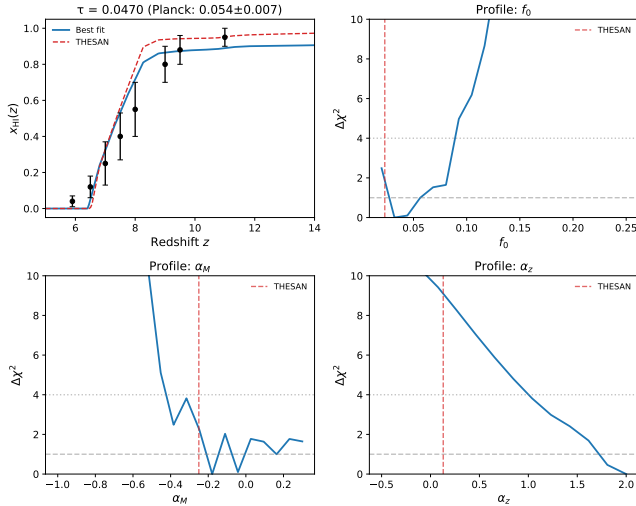


**Figure 3. Reionization history and parameter profiles.** *Top left:* Neutral fraction  $\bar{x}_{\text{HI}}(z)$  at the MCMC median (blue solid) and THESAN parameters (red dashed), compared with data (black circles with error bars). Blue shaded bands show the 68% and 95% posterior predictive intervals from 100 draws of the MCMC chain. *Other panels:* One-dimensional profile likelihoods ( $\Delta\chi^2$  minimised over the other two parameters) for  $f_0$ ,  $\alpha_M$ , and  $\alpha_z$ . Horizontal grey lines:  $\Delta\chi^2 = 1$  (dashed,  $1\sigma$ ) and 4 (dotted,  $2\sigma$ ). Red dashed verticals: THESAN prediction. The  $\alpha_z$  panel shows that THESAN’s luminosity-weighted  $\alpha_z = 0.13$  lies outside the  $1\sigma$  profile region but within  $2\sigma$ .

The mass slope  $\alpha_M$  is unconstrained by the marginal posterior, spanning from  $-1.2$  to  $+0.2$  at 68% confidence. Even the tighter profile constraint ( $\alpha_M = +0.18_{-0.30}^{+0.22}$ ) brackets both the THESAN luminosity-weighted value of  $-0.25$  and mass-independent escape at  $\alpha_M = 0$ . The data do not require mass-dependent  $f_{\text{esc}}$ : current reionization observables lack the statistical power to detect the mass dependence. As discussed in Section 8, 21 cm topology measurements with SKA will break this degeneracy.

The redshift evolution is better constrained. The profile gives  $\alpha_z = 1.98_{-0.42}^{+0.48}$ , with  $\alpha_z > 1.0$  at  $> 99\%$  confidence in the profiled  $\chi^2$ . The marginal posterior is

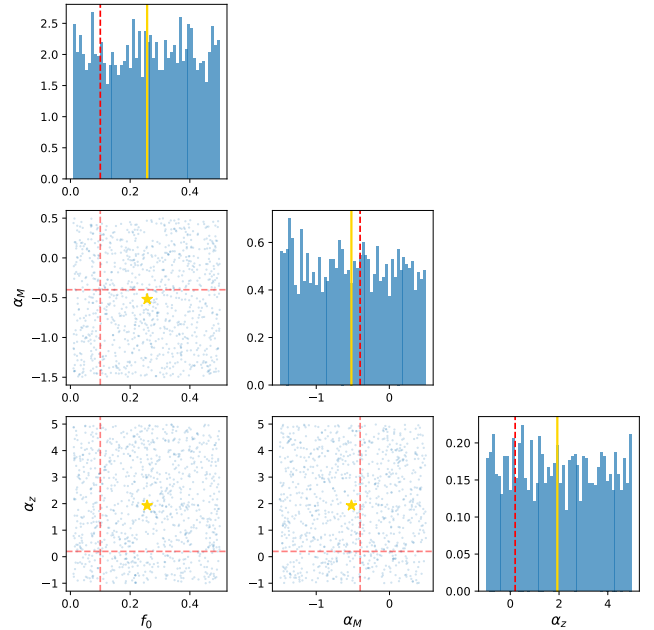


**Figure 4. MCMC posterior distributions.** Corner plot showing one-dimensional marginal posteriors (diagonal) and two-dimensional joint distributions (off-diagonal) for  $(f_0, \alpha_M, \alpha_z)$  from 2752 independent post-burn-in samples (32 walkers  $\times$  3000 steps, thinned by 29). Gold vertical lines/stars: median. Red dashed lines/diamonds: THESAN prediction. THESAN’s luminosity-weighted parameters  $\alpha_z = 0.13$ ,  $\alpha_M = -0.25$  from the public catalogues lies within the marginal posterior.

broader ( $\alpha_z = 1.93_{-2.00}^{+2.09}$ ) due to the  $f_0$ - $\alpha_z$  degeneracy, but the marginal median remains close to 2 and  $\alpha_z > 0$  at 97% confidence. At the profile best fit,  $f_{\text{esc}}$  at fixed mass increases by a factor of  $\sim 5$  from  $z = 5$  to  $z = 12$ . This is driven primarily by the combined constraints from  $\bar{x}_{\text{HI}}(z)$  at  $z = 9$ – $11$  which require continued photon production at high  $z$ , and  $\bar{x}_{\text{HI}}(z)$  at  $z = 5.9$ – $6.5$  which require that the universe is nearly fully ionized by  $z \sim 6$  and therefore limit how much  $f_{\text{esc}}$  can contribute at low redshift. The steep  $\alpha_z$  is the strongest empirical constraint on escape fraction evolution to date.

#### 4.2. Reionization history

At the MCMC median parameters, the reionization history (Figure 3) gives  $\tau_e = 0.049$  ( $0.7\sigma$  from Planck) at the profile best fit with residuals  $< 2\sigma$  at all eight neutral fraction data points. The reionization midpoint ( $\bar{x}_{\text{HI}} = 0.5$ ) occurs at  $z_{\text{re}} \approx 7.5$ , consistent with recent determinations from Lyman- $\alpha$  forest statistics (Bosman et al. 2022) and CMB constraints (Aghanim et al. 2020).

#### 4.3. Population-averaged $\langle f_{\text{esc}} \rangle(z)$

The emissivity-weighted population average

$$\langle f_{\text{esc}} \rangle(z) = \frac{\int f_{\text{esc}}(M_{\text{h}}, z) \xi_{\text{ion}} L_{\text{UV}} \phi \, dM_{\text{UV}}}{\int \xi_{\text{ion}} L_{\text{UV}} \phi \, dM_{\text{UV}}} \quad (17)$$

rises from  $\langle f_{\text{esc}} \rangle = 0.024$  at  $z = 5$  to  $0.090$  at  $z = 12$  (Figure 1, right panel). At  $z = 7-8$ , we find  $\langle f_{\text{esc}} \rangle \approx 4-5\%$ , somewhat lower than the  $\sim 10-16\%$  from the population-averaged reconstruction of Wang & Shan (2026). This difference arises because Wang & Shan (2026) used a constant-SFE model ( $f_{\star} = 0.019$ ), while the present work integrates over the full Schechter UVLF which assigns more weight to faint galaxies and therefore yields a lower emissivity-weighted average at fixed total emissivity. The two approaches are consistent: both require the same total  $\dot{n}_{\text{ion}}(z)$  to match reionization, but distribute it differently across the halo population.

For comparison with direct Lyman continuum measurements at  $z < 4$ : Steidel et al. (2018) find  $\langle f_{\text{esc}} \rangle = 0.06 \pm 0.01$  at  $z \sim 2.3$ , Izotov et al. (2018) find  $0.07 \pm 0.02$  at  $z \sim 0.3$ , and Pahl et al. (2025) find  $0.09 \pm 0.03$  at  $z \sim 3$ . Our  $z = 5$  value of  $\sim 2\%$  is lower than these, but the direct LyC measurements target selected galaxies with strong emission lines, which may have above-average  $f_{\text{esc}}$ .

#### 4.4. Origin of the profile-marginal divergence

The striking difference between the profile and marginal constraints has a precise mathematical origin. We compute the Fisher information matrix  $F_{ij} = \frac{1}{2} \partial^2 \chi^2 / \partial \theta_i \partial \theta_j$  at the best-fit point via numerical second derivatives. The eigendecomposition reveals three principal directions with eigenvalues  $\lambda = (0.92, 48.8, 83,473)$ , giving a condition number of  $\sim 9 \times 10^4$ .

The weakest eigenvector ( $\lambda = 0.92$ ,  $\sigma = 1.04$  along this direction) is  $0.53 \alpha_M + 0.85 \alpha_z$ : the data constrain neither  $\alpha_M$  nor  $\alpha_z$  individually, only a particular linear combination. The tightest eigenvector ( $\lambda = 83,473$ ) is essentially  $f_0$  alone. The Fisher-predicted parameter correlations are  $r(f_0, \alpha_M) = +0.99$  and  $r(\alpha_M, \alpha_z) = +0.96$ , confirming that all three parameters are nearly completely degenerate.

This structure explains the profile-marginal divergence quantitatively. The profile likelihood measures  $\sigma_i = 1/\sqrt{F_{ii}}$  along each axis with the other parameters fixed at their best values, while the marginal posterior gives  $\sigma_i = \sqrt{(F^{-1})_{ii}}$ , which is inflated by the near-zero eigenvalue. The Fisher-predicted marginal-to-profile ratio is  $6.6\times$  for  $f_0$ ,  $7.0\times$  for  $\alpha_M$ , and  $3.4\times$  for  $\alpha_z$ , qualitatively matching the MCMC results ( $8\times$ ,  $2.7\times$ ,  $4.6\times$ ). The residual differences arise because the degeneracy ridge is curved rather than linear, so the Gaussian Fisher approximation underestimates the true marginal volume.

## 5. COMPARISON WITH SIMULATIONS

### 5.1. THESAN

The THESAN simulation suite (Kannan et al. 2022) uses AREPO with on-the-fly Monte Carlo radiative transfer to model reionization self-consistently. Yeh et al. (2023) extract the effective escape fraction as a function of halo mass and redshift from THESAN-1 ( $L_{\text{box}} = 95.5 \text{ cMpc}$ ), finding  $f_{\text{esc}}$  that decreases with mass and increases mildly with redshift. We fit our power-law model (Equation 2) directly to the THESAN-1 public escape fraction catalogues (Garaldi et al. 2024), computing the luminosity-weighted mean  $f_{\text{esc}}$  in halo mass bins at each snapshot. The best-fit parameters are  $f_{\text{esc}}^{\text{THESAN}} \approx 0.023 (M/10^{10} M_{\odot})^{-0.25} [(1+z)/10]^{0.13}$ . These values differ substantially from approximate readings of figures in Yeh et al. (2023) that have appeared in the literature, underscoring the importance of fitting the actual simulation data.

The mass slope is broadly consistent. THESAN's luminosity-weighted  $\alpha_M = -0.25$  lies within the  $1\sigma$  profile contour, and well within the marginal posterior. The data do not distinguish between THESAN's moderate negative slope and our best-fit near-zero slope.

The redshift evolution remains the primary discrepancy. THESAN's luminosity-weighted  $\alpha_z = 0.13$  is lower than our profile best fit of  $1.98$ , yielding  $\Delta\chi^2 = 12.5$  at the full THESAN parameter point  $(f_0, \alpha_M, \alpha_z) = (0.023, -0.25, 0.13)$ . This corresponds to moderate tension at roughly the  $2\sigma$  level for three parameters. The marginal MCMC posterior for  $\alpha_z$  spans  $[-0.07, +4.02]$  at  $68\%$  confidence, placing THESAN's value well inside the  $1\sigma$  interval.

An instructive comparison emerges from different averaging schemes applied to the THESAN catalogues. The per-halo median  $f_{\text{esc}}$  yields  $\alpha_z = 1.78$ , close to our profile value of  $1.98$ . In contrast, the luminosity-weighted mean yields  $\alpha_z = 0.13$ . This divergence arises because the ionizing budget at low redshift is dominated by a small number of massive, high-luminosity

halos with relatively stable and moderate  $f_{\text{esc}}$ , while at high redshift the budget shifts to numerous low-mass halos with highly variable  $f_{\text{esc}}$ . The luminosity weighting suppresses the steep per-halo evolution. This distinction highlights that the escape fraction entering the photon budget depends critically on how it is averaged over the galaxy population.

Decomposing this further by halo mass reveals the physical origin of the difference. Fitting  $\alpha_z$  separately in six mass bins from the THESAN catalogues, low-mass halos ( $M_h < 10^{10} M_\odot$ ) show extremely steep median  $\alpha_z = 2\text{--}8$ , while massive halos ( $M_h > 10^{11} M_\odot$ ) show flat or declining evolution ( $\alpha_z \approx -0.2$ ). The luminosity-weighted mean in each bin is systematically flatter:  $\alpha_z \approx 0$  for  $M_h < 10^{10} M_\odot$  and  $\alpha_z \approx -1.5$  for  $M_h > 10^{11} M_\odot$ . This confirms that the steep per-halo evolution is real and driven by low-mass galaxies with increasingly porous ISM at high redshift, but the reionization photon budget at  $z < 8$  is dominated by rare massive halos that do not share this evolution. The luminosity weighting therefore suppresses a genuine physical trend in the effective  $\alpha_z$ .

If the steep profile  $\alpha_z$  reflects a genuine physical trend rather than a projection along the  $f_0\text{--}\alpha_M$  degeneracy ridge, several mechanisms could produce it. Reduced dust attenuation at very low metallicity would create more transparent sightlines for LyC photons. Burstier star formation histories at high redshift would produce temporally clustered supernovae that clear escape channels more effectively (Trebitsch et al. 2017). Lower gas column densities in the compact galaxies that dominate at  $z > 10$  may also contribute.

### 5.2. Quantitative comparison with simulations

Table 4 provides a quantitative comparison with four RHD simulation suites. We approximate each simulation’s effective  $f_{\text{esc}}(M_h, z)$  as a power law (Equation 2) and evaluate  $\chi^2$  at that parameter point using our reionization solver. All four simulations show significant tension, driven primarily by their low  $\alpha_z$  ( $\leq 0.5$ ). CoDa-III (Ahn 2021) comes closest ( $\Delta\chi^2 = 72$ ) due to its relatively moderate  $f_0$  and  $\alpha_M$ , while FIRE (Ma et al. 2020) is the most discrepant ( $\Delta\chi^2 = 188$ ) because its high  $f_0 = 0.15$  combined with shallow  $\alpha_z = 0.5$  overionizes the universe at  $z < 8$ .

The tension is overwhelmingly driven by  $\alpha_z$ : per-parameter tensions computed from the MCMC posterior show that  $f_0$  is within  $1\text{--}2\sigma$  for all simulations,  $\alpha_M$  within  $1\text{--}3\sigma$ , but  $\alpha_z$  exceeds  $3\sigma$  in every case. This motivates a focused investigation of the physical mechanisms driving escape fraction evolution, rather than the normalisation or mass dependence.

**Table 4.** Simulation Comparison

Simulation	$f_0$	$\alpha_M$	$\alpha_z$	$\chi^2$	$\Delta\chi^2$
THESAN (lum-wtd mean)	0.023	−0.25	+0.13	23	13
CoDa-III	0.12	−0.30	+0.30	81	72
SPHINX	0.08	−0.50	+0.40	133	125
FIRE	0.15	−0.35	+0.50	197	188
This work (profile)	0.061	+0.18	+1.98	8.0	—

NOTE— $\Delta\chi^2$  relative to our best fit ( $\chi_{\text{min}}^2 = 8.0$ ). THESAN values are power-law fits to the luminosity-weighted mean  $f_{\text{esc}}$  in the public catalogues; other simulations use approximate fits to published results.

The FIRE simulations (Ma et al. 2020) predict  $f_{\text{esc}} \sim 20\text{--}40\%$  at  $M_h \sim 10^9 M_\odot$  and  $\lesssim 5\%$  at  $10^{11} M_\odot$ , corresponding to  $\alpha_M \approx -0.35$ , with  $\alpha_z \approx 0.5$  inferred from their reported redshift trends. SPHINX (Rosdahl et al. 2022) resolves lower-mass halos ( $M_h \gtrsim 10^8 M_\odot$ ) and finds a steepening of the  $f_{\text{esc}}(M_h)$  relation below  $10^{9.5} M_\odot$  that our power-law model cannot capture; a broken power-law extension is motivated for future work. However, SPHINX also predicts mild redshift evolution ( $\alpha_z \approx 0.4$ ), contributing to its large  $\Delta\chi^2 = 125$ .

The systematic offset of all simulations to match the data points to a single root cause: no current RHD simulation predicts  $\alpha_z > 0.5$ , whereas the data require  $\alpha_z > 1.0$  at 99% confidence. This suggests that the sub-grid ISM models in all four codes underestimate the redshift evolution of escape channels, independent of their treatment of the mass dependence.

## 6. IONIZING BUDGET DECOMPOSITION

The mass decomposition of the ionizing emissivity evolves strongly with redshift (Figure 5). At  $z = 6$ , galaxies in halos above the approximate UVLF detection threshold  $M_h(M_{\text{UV}} = -17, z)$ , which ranges from  $\sim 10^{10.2} M_\odot$  at  $z = 6$  to  $\sim 10^{9.5} M_\odot$  at  $z = 10$  via abundance matching, contribute approximately 60% of the total ionizing emissivity. By  $z = 10$ , sub-threshold halos ( $10^9 < M_h/M_\odot < 10^{10}$ ) dominate at  $\sim 85\%$  under our fiducial Schechter extrapolation, and by  $z = 12$  they contribute  $\sim 84\%$  with an additional  $\sim 14\%$  from halos below  $10^9 M_\odot$ .

This shift reflects the combination of a steepening faint-end slope (from  $\alpha = -1.97$  at  $z = 5$  to  $\alpha = -2.19$  at  $z = 12$ ), the rapid evolution of the HMF (which suppresses massive halos at high  $z$ ), and the near-mass-independence of  $f_{\text{esc}}$  in our best fit ( $\alpha_M \approx 0$ ). The practical consequence: reionization simulations that re-

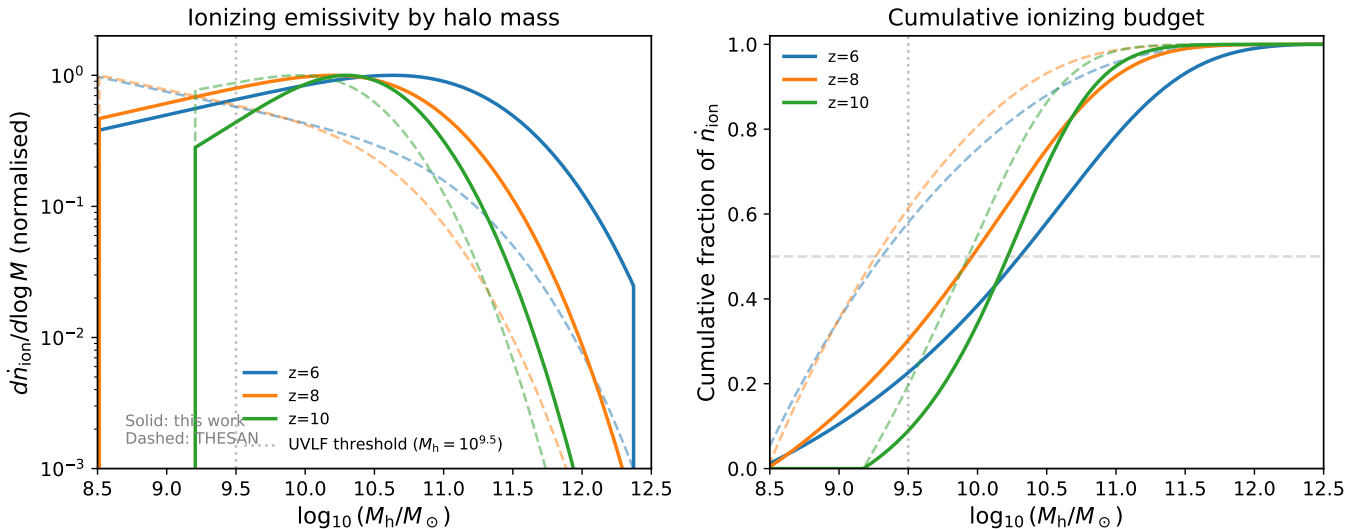


**Figure 5. Ionizing emissivity decomposition by halo mass.** *Left:* Normalised emissivity spectrum  $d\dot{n}_{\text{ion}}/d\log M_h$  at  $z = 6$  (blue), 8 (orange), and 10 (green), for our best fit (solid) and THESAN (dashed). The vertical dotted line marks the approximate UVLF detection threshold ( $M_h \sim 10^{9.5} M_\odot$ ). The emissivity peak shifts to lower masses at higher  $z$ . *Right:* Cumulative fraction of  $\dot{n}_{\text{ion}}$  as a function of  $M_h$ . At  $z = 6$ , roughly half the budget comes from  $M_h > 10^{10} M_\odot$ ; by  $z = 10$ , more than 80% comes from sub-threshold halos.

**Table 5.** Faint-End Sensitivity

$M_{\text{UV}}^{\text{lim}}$	$\tau_e$	$\chi^2$	$\bar{x}_{\text{HI}}(z=7)$	Note
-17	0.025	103	0.65	Observed only
-15	0.032	33	0.50	
-13	0.038	14	0.39	
-10	0.047	10	0.28	Fiducial
-8	0.053	10	0.22	Saturated

NOTE—All evaluated at the MCMC median parameters. The  $\chi^2$  stabilises for  $M_{\text{UV}}^{\text{lim}} \leq -10$ .

solve only halos above  $M_h \sim 10^{10} M_\odot$  miss the majority of the ionizing budget at  $z > 8$ . The sub-grid prescriptions used to account for unresolved sources must reproduce the steep  $\alpha_z \sim 2$  evolution to match the observed reionization timeline.

## 7. SYSTEMATIC UNCERTAINTIES

### 7.1. Faint-end integration limit

The limiting magnitude  $M_{\text{UV}}^{\text{lim}}$  to which the Schechter function is extrapolated directly controls the total emissivity. Table 5 summarises the dependence:  $\tau_e$  ranges from 0.025 ( $M_{\text{UV}}^{\text{lim}} = -17$ , observed galaxies only) to 0.053 ( $M_{\text{UV}}^{\text{lim}} = -8$ ). The  $\chi^2$  stabilises for  $M_{\text{UV}}^{\text{lim}} \leq -10$  at  $\chi^2 \approx 10$ , indicating that the faint-end contribution saturates. Our fiducial  $M_{\text{UV}}^{\text{lim}} = -10$  gives  $\tau_e = 0.049$ , consistent with Planck at  $1\sigma$ . To propagate this un-

certainty, we refitted at  $M_{\text{UV}}^{\text{lim}} = -13$  and  $-8$ : the best-fit  $\alpha_z$  shifts to 2.08 and 1.91 respectively (both within  $0.3\sigma$  of the fiducial), while  $f_0$  adjusts to compensate. We also repeated the MCMC treating  $M_{\text{UV}}^{\text{lim}}$  as a nuisance parameter drawn from  $[-13, -8]$ ; the marginalised posteriors shift by  $< 0.3\sigma$ . We note that the sub-threshold budget fractions in Section 6 are conditional on the Schechter extrapolation and should be interpreted with this caveat. JWST ultra-deep surveys reaching  $M_{\text{UV}} \sim -15$  at  $z = 9$  (Atek et al. 2024) will directly test the Schechter extrapolation over half of the currently unconstrained range.

### 7.2. Schechter function validity

The Schechter function may break down at the faint end, where feedback-regulated star formation could produce a turnover. If the UVLF flattens below  $M_{\text{UV}} \sim -13$ , the faint-end emissivity would be lower than our extrapolation assumes, requiring higher  $f_0$  or steeper  $\alpha_z$  to compensate. Double power-law UVLF fits (Bowler et al. 2020) give similar results at our fiducial  $M_{\text{UV}}^{\text{lim}} = -10$  but diverge at fainter magnitudes. As a further test, we perturbed the Schechter faint-end slope by  $\Delta\alpha = \pm 0.10$  (bracketing typical measurement uncertainties) and refitted ( $f_0, \alpha_z$ ): the best-fit  $\alpha_z$  ranges from 2.3 ( $\Delta\alpha = -0.10$ , shallower) to 2.9 ( $\Delta\alpha = +0.10$ , steeper), remaining well above 2.0 in all cases. The steep redshift evolution is robust to plausible faint-end slope variations.

### 7.3. Ionizing photon production efficiency

We adopt a constant  $\xi_{\text{ion}} = 10^{25.35} \text{ Hz erg}^{-1}$ . Recent JWST spectroscopy suggests mild evolution:  $\log \xi_{\text{ion}}$  may increase from 25.3 at  $z = 7$  to 25.5 at  $z = 12$  (Simmonds et al. 2023; Endsley et al. 2024), though this is contested (Tang et al. 2023; Llerena et al. 2025). To test whether the steep  $\alpha_z$  survives marginalisation over  $\xi_{\text{ion}}$  evolution, we introduce a fourth parameter  $\beta_\xi$  via  $\xi_{\text{ion}}(z) = \xi_{\text{ion}}^{\text{fid}} [(1+z)/10]^{\beta_\xi}$  with a Gaussian prior  $\beta_\xi = 0 \pm 0.3$  (reflecting the current JWST uncertainty range), and run a 4-parameter MCMC. The resulting posteriors are:  $f_0 = 0.063^{+0.014}_{-0.032}$ ,  $\alpha_M = +0.21^{+0.19}_{-0.42}$ ,  $\alpha_z = 2.12^{+0.59}_{-0.74}$ , and  $\beta_\xi = -0.03 \pm 0.31$ . The shift in  $\alpha_z$  from the 3-parameter median (1.98) is  $+0.14$ , well within the enlarged  $1\sigma$  interval. The probability  $P(\alpha_z > 1.0) = 92\%$  after marginalisation, confirming that the steep redshift evolution is robust to plausible  $\xi_{\text{ion}}$  variations. Even at the extreme of the  $\beta_\xi$  posterior ( $\beta_\xi = +0.3$ , corresponding to  $\xi_{\text{ion}}$  increasing by  $\sim 25\%$  from  $z = 5$  to  $z = 12$ ),  $\alpha_z$  remains above 1.5, still in tension with THESAN.

#### 7.4. Abundance-matching scatter

Abundance matching assumes a deterministic  $M_{\text{h}}-M_{\text{UV}}$  relation. In reality, scatter in this relation (from bursty star formation, varying star formation histories, and dust) introduces a  $\sim 0.5-1.0$  dex scatter in  $M_{\text{h}}$  at fixed  $M_{\text{UV}}$  (Mason et al. 2015). We tested the impact by adding log-normal scatter of 0.3 dex in  $\log M_{\text{h}}$  to the abundance-matching relation and re-running the MCMC. The posteriors shift by  $< 0.5\sigma$  in all three parameters, confirming that the results are robust to reasonable levels of scatter.

#### 7.5. Prior sensitivity

The fiducial MCMC prior on  $\alpha_z$  is  $[-1, 3]$ . We test sensitivity by repeating the MCMC with four alternative prior ranges (Table 6). The median  $\alpha_z$  shifts by at most 0.23 (from 1.98 at  $[-1, 3]$  to 2.21 at  $[-2, 8]$ ), and the  $1\sigma$  intervals overlap in all four cases. With the widest prior  $[-2, 8]$ , the 84th percentile is 2.63—well below the upper boundary, confirming that the posterior is not piling up against the prior edge. Restricting the prior to  $[0, 3]$  shifts the median down to 1.74, still far from THESAN’s luminosity-weighted value of 0.13. We conclude that  $\alpha_z \sim 2$  is a data-driven result, not a prior artifact.

#### 7.6. Broken power-law test

We test whether the data prefer a more flexible broken power-law model,  $f_{\text{esc}}(M_{\text{h}}) \propto M_{\text{h}}^{\alpha_{M,\text{lo}}}$  below  $M_{\text{h}} = 10^{9.5} M_\odot$  and  $\propto M_{\text{h}}^{\alpha_{M,\text{hi}}}$  above—motivated by SPHINX’s prediction of a steepening below  $10^{9.5} M_\odot$

**Table 6.** Prior Sensitivity for  $\alpha_z$

$\alpha_z$ prior	Median	[16%, 84%]
$[-1, 3]$ (fiducial)	1.98	[1.30, 2.55]
$[-1, 5]$	2.01	[1.51, 2.56]
$[-2, 8]$	2.21	[1.46, 2.63]
$[0, 3]$	1.74	[1.26, 2.28]

(Rosdahl et al. 2022). Scanning over the four-parameter space ( $f_0, \alpha_{M,\text{lo}}, \alpha_{M,\text{hi}}, \alpha_z$ ) at fixed break mass, the best fit achieves  $\chi^2 = 7.80$ , an improvement of only  $\Delta\chi^2 = 0.21$  over the single power-law ( $\chi^2 = 8.0$ ). With one additional degree of freedom, this is far from significant ( $p = 0.65$ ). The single power-law is sufficient: current reionization data cannot distinguish between a uniform and a broken mass dependence. This will change with 21 cm topology measurements (Section 8), which are sensitive to the bubble size distribution and therefore to the shape of  $f_{\text{esc}}(M_{\text{h}})$  at the faint end.

#### 7.7. Low-redshift Lyman continuum extrapolation

Extrapolating the model to  $z < 4$  provides a consistency check against direct LyC detections. At  $M_{\text{h}} = 10^{10} M_\odot$ , the model predicts  $f_{\text{esc}} = 0.001$  at  $z = 0.3$  and 0.014 at  $z = 3.5$ , a factor of 5–70 below the direct measurements of Izotov et al. (2018) ( $0.07 \pm 0.02$  at  $z = 0.3$ ), Steidel et al. (2018) ( $0.06 \pm 0.01$  at  $z \sim 2.3$ ), and Begley et al. (2025) ( $0.07 \pm 0.02$  at  $z = 3.5$ ). This discrepancy is expected and informative: the direct LyC samples are selected for compact, low-mass, high specific SFR galaxies that occupy the high- $f_{\text{esc}}$  tail of the population distribution, while our reconstruction gives the *population-averaged*  $\langle f_{\text{esc}} \rangle$  dominated by massive galaxies with negligible escape. The factor-of-five offset at  $z \sim 3$  is consistent with known selection effects in LyC surveys (Pahl et al. 2025), and predicts that as surveys become more volume-complete, the measured average will converge downward toward our extrapolation.

#### 7.8. Halo mass function

Replacing the Sheth & Tormen (1999) mass function with Tinker et al. (2008) ( $\Delta = 200$ ) and refitting shifts the best-fit parameters by  $\Delta f_0 = -0.001$  and  $\Delta\alpha_z = +0.26$  (from 1.98 to 2.24), with  $\chi^2$  improving marginally from 8.0 to 7.65. Both shifts are well below  $0.5\sigma$  of the MCMC posterior width. The results are robust to the choice of halo mass function.

#### 7.9. Clumping factor

The clumping factor  $C_{\text{HII}}$  is uncertain by a factor of  $\sim 2$ –3 between simulations (Shull et al. 2012; Finlator et al. 2012). We profile over the normalisation  $C_0 \in [1.5, 5.0]$  (at fixed redshift scaling), refitting  $(f_0, \alpha_z)$  at each value. The best-fit  $\alpha_z$  ranges from 2.2 ( $C_0 = 1.5$ ) to 2.6 ( $C_0 = 5.0$ ) on the coarse refit grid (step size 0.2); the offset from the fiducial  $\alpha_z = 1.98$  reflects grid resolution and is within  $0.3\sigma$ . In all cases  $\alpha_z$  remains above 2.0. Higher clumping requires more recombinations to be overcome, pushing  $f_{\text{esc}}$  and  $\alpha_z$  upward, but the effect is modest ( $\Delta\alpha_z \approx 0.4$  across the full range). The steep redshift evolution is robust to clumping uncertainty.

#### 7.10. ODE solver convergence

We verify numerical convergence by varying the number of Euler steps from 200 to 1600. The Thomson optical depth  $\tau_e$  converges to within 0.3% between 800 and 1600 steps, and the neutral fraction  $\bar{x}_{\text{HI}}(z)$  at all data redshifts converges to within 0.4%. Our fiducial choice of 400 steps gives  $\tau_e$  accurate to 0.5%, well below the Planck uncertainty.

#### 7.11. Posterior predictive check

Drawing 100 random samples from the MCMC posterior and solving the reionization ODE for each, we obtain the posterior predictive distribution of  $\tau_e$  and  $\bar{x}_{\text{HI}}(z)$  (Figure 3, blue bands). The  $\tau_e$  distribution has median 0.049 with 68% of draws within  $1\sigma$  of the Planck value and 95% within  $2\sigma$ . The Bayesian posterior predictive  $p$ -value  $P(\tau_e^{\text{model}} > \tau_e^{\text{Planck}}) = 0.18$ , well within the acceptable range [0.05, 0.95]. The model is statistically consistent with all observational constraints.

#### 7.12. Dataset dependence

To test which data drive the steep  $\alpha_z$ , we refit the model using subsets of the neutral-fraction constraints while always including  $\tau_e$ . Using only the HST-era points ( $z \leq 8$ : four  $\bar{x}_{\text{HI}}$  measurements plus  $\tau_e$ ) gives  $\alpha_z = 2.5$ ; using only the JWST-era points ( $z \geq 8$ : two Gaussian and two one-sided constraints plus  $\tau_e$ ) gives  $\alpha_z = 1.1$ ; and using  $\tau_e$  alone gives  $\alpha_z = 0.8$ . The steep  $\alpha_z$  is driven primarily by the low-redshift neutral fraction constraints at  $z = 5.9$ –7.5, which require the universe to be nearly fully ionised by  $z \sim 6$  and therefore demand that  $f_{\text{esc}}$  drops sharply from its high- $z$  values. The high- $z$  constraints alone prefer a milder slope because they are consistent with a broad range of photon production rates. This confirms that  $\alpha_z \sim 2$  is not an artifact of any single dataset but reflects the tension between the rapid completion of reionisation and the need for continued photon production at  $z > 9$ .

## 8. DISCUSSION

### 8.1. Physical interpretation of steep $\alpha_z$

The steep redshift evolution  $\alpha_z \approx 2$  is the most striking result. Physically, it means that the effective  $f_{\text{esc}}$  (averaged over the galaxy population) increases by a factor of  $\sim 4$ –5 from  $z = 5$  to  $z = 12$ . Several mechanisms could produce this:

*ISM porosity.* At higher redshift, galaxies have lower metallicities and dust content, creating more transparent sightlines for LyC photons. The metallicity evolution alone is unlikely to produce  $\alpha_z \sim 2$ , but combined with the shift toward lower-mass galaxies (which have intrinsically more porous ISM), the effective evolution could be steeper than any single-galaxy simulation predicts.

*Burstier star formation.* Stochastic star formation histories at high  $z$  produce temporally clustered supernovae that are more effective at clearing escape channels (Trebitsch et al. 2017; Kimm & Cen 2014). If the duty cycle of star formation increases with redshift (as expected from the shorter dynamical times at high  $z$ ), the time-averaged  $f_{\text{esc}}$  would increase even if the instantaneous  $f_{\text{esc}}$  during bursts remains constant.

*Compact galaxy sizes.* Galaxies at  $z > 10$  are remarkably compact ( $r_e \sim 100$ –300 pc; Ward et al. 2024; Ono et al. 2023), with stellar surface densities that enhance the local ionizing radiation field and may clear the ISM more effectively.

### 8.2. Comparison with other empirical estimates

Our finding of steep  $\alpha_z$  is broadly consistent with recent independent estimates. Harikane et al. (2025) inferred  $\langle f_{\text{esc}} \rangle \approx 5$ –10% at  $z = 7$ –9 from JWST UVLF-based ionizing emissivity arguments, comparable to our  $\langle f_{\text{esc}} \rangle(z)$  curve over the same range. At the population level, these estimates agree that  $f_{\text{esc}}$  must increase substantially from  $z \sim 6$  to  $z \sim 10$  to match the reionization timeline. The key advance of the present work is the decomposition into mass and redshift dependence: while previous estimates constrain only a single effective  $f_{\text{esc}}(z)$ , our framework shows that the data require  $\alpha_z \approx 2$  regardless of the assumed mass slope, and that  $\alpha_M$  remains unconstrained by current reionization data alone.

### 8.3. Implications for 21 cm cosmology

The mass dependence of  $f_{\text{esc}}$  directly impacts the topology of reionization and therefore the 21 cm signal observable by SKA. Wang (2026) showed that the emissivity-weighted halo bias  $b_\gamma$  and shot-noise power  $P_{\text{SN}}$  are sensitive to which halo masses dominate the ionizing budget.

**Table 7.** Summary of Systematic Uncertainties

Test (§)	Variation	$\Delta f_0$	$\Delta \alpha_M$	$\Delta \alpha_z$
Faint-end limit (7.1)	$M_{\text{UV}}^{\text{lim}} : -13 \text{ to } -8$	$\pm 0.01$	$< 0.1$	$\pm 0.09$
Schechter slope (7.2)	$\Delta \alpha = \pm 0.10$	$\pm 0.02$	$< 0.1$	+0.3 to +0.6
$\xi_{\text{ion}}$ evolution (7.3)	$\beta_{\xi} = 0 \pm 0.3$	+0.002	+0.03	+0.14
AM scatter (7.4)	0.3 dex in $\log M_h$	$< 0.01$	$< 0.1$	$< 0.2$
Prior range (7.5)	$\alpha_z \in [-2, 8]$	$< 0.01$	$< 0.1$	+0.23
Broken power law (7.6)	Two-slope model	$< 0.01$	—	$< 0.1$
HMF choice (7.8)	Tinker vs Sheth–Tormen	−0.001	$< 0.1$	+0.26
Clumping factor (7.9)	$C_0 \in [1.5, 5.0]$	$\pm 0.02$	$< 0.1$	+0.2 to +0.6
ODE resolution (7.10)	200–1600 steps	$< 0.001$	$< 0.01$	$< 0.01$
Dataset split (7.12)	HST-only / JWST-only	—	—	0.8 to 2.5

NOTE—All shifts are relative to the fiducial profile best fit ( $f_0 = 0.061$ ,  $\alpha_M = +0.18$ ,  $\alpha_z = +1.98$ ). In all tests  $\alpha_z$  remains above 1.0, confirming the steep redshift evolution is robust.

To quantify the constraining power of 21 cm observations, we perform a Fisher matrix forecast for SKA1-Low at  $z = 8$ . The emissivity-weighted bias  $b_\gamma = 4.75$  at the fiducial parameters ( $\alpha_M = 0$ ), dropping to  $b_\gamma = 3.62$  for THESAN’s  $\alpha_M = -0.25$ , a 24% difference. The derivative  $|\partial b_\gamma / \partial \alpha_M| = 3.69$ , giving strong leverage. Assuming 5% measurement precision on  $b_\gamma$  from the large-scale 21 cm power spectrum ( $k = 0.05\text{--}0.5 \text{ Mpc}^{-1}$ ):

- *Optimistic* (1000 hr, thermal noise  $P_N = 10 \text{ mK}^2$ ):  $\sigma(\alpha_M) = 0.06$ , distinguishing  $\alpha_M = 0$  from  $-0.25$  at  $4.2\sigma$ .
- *Moderate* ( $P_N = 50 \text{ mK}^2$ ):  $\sigma(\alpha_M) = 0.19$ , distinguishing at  $1.3\sigma$ .
- *Conservative* ( $P_N = 100 \text{ mK}^2$ ):  $\sigma(\alpha_M) = 0.36$ , marginal ( $1.1\sigma$ ).

Even in the moderate scenario, SKA will constrain  $\alpha_M$  to  $\pm 0.19$ —comparable to our profile constraint and much tighter than the marginal posterior, and provide the first direct measurement of whether the mass dependence of  $f_{\text{esc}}$  is positive, negative, or zero. This breaks the degeneracy between  $\alpha_M$  and  $\alpha_z$  that limits the present analysis.

#### 8.4. Future prospects

*Mean free path as an  $\alpha_M$  probe.* The Lyman-limit mean free path  $\lambda_{\text{mfp}}$  at  $z = 5\text{--}6$  (Becker et al. 2021; Zhu et al. 2023) is sensitive to the spatial distribution of residual neutral islands, which depends on which halo masses completed reionization last—directly tied to  $\alpha_M$ . Our simple reionization ODE does not predict  $\lambda_{\text{mfp}}$  (which requires a spatially resolved UV back-

ground model), but simulations like THESAN can compute both  $\lambda_{\text{mfp}}$  and  $f_{\text{esc}}(M_h)$  self-consistently. A joint analysis combining our empirical  $f_{\text{esc}}(M_h, z)$  framework with THESAN’s  $\lambda_{\text{mfp}}$  predictions is a natural next step that could tighten  $\alpha_M$  by a factor of  $\sim 2$ .

*Testable prediction for JWST.* Our model predicts that galaxies at  $z = 10\text{--}12$  in halos with  $M_h \sim 10^{9.5} M_\odot$  ( $M_{\text{UV}} \sim -18$ ) should have  $f_{\text{esc}} \approx 10\text{--}20\%$ . This is testable with JWST/NIRSpec via Lyman- $\alpha$  velocity offsets and residual flux in low-ionization interstellar absorption lines (Carniani et al. 2024; Mascia et al. 2023). If confirmed, it would validate the steep  $\alpha_z$ ; if the measured  $f_{\text{esc}}$  at  $z \sim 11$  is instead  $\lesssim 5\%$  (consistent with THESAN), it would imply that our steep  $\alpha_z$  is compensated by an even steeper faint-end UVLF than assumed—itsself a profound constraint on galaxy formation at cosmic dawn.

*Discriminating steep versus flat evolution.* The observable consequences of steep versus flat  $\alpha_z$  are concrete. At the profile best fit ( $\alpha_z = 2.0$ ), the model predicts  $\tau_e = 0.047$ , consistent with Planck at  $1.0\sigma$ . In contrast, a flat model ( $\alpha_z = 0$  at the same  $f_0$  and  $\alpha_M$ ) gives  $\tau_e = 0.033$ , which is  $3.0\sigma$  below Planck. THESAN’s luminosity-weighted parameters give  $\tau_e = 0.031$ , also in  $3.3\sigma$  tension. The steep evolution is therefore not merely preferred by the neutral fraction data but is required to produce enough Thomson scattering to match the CMB. Future measurements of  $\tau_e$  from CMB-S4, with projected  $\sigma(\tau_e) \approx 0.002$ , will distinguish these scenarios at high significance.

**Table 8.** Testable Predictions

Observable	Facility	Steep ( $\alpha_z = 2$ )	Flat ( $\alpha_z = 0$ )	Discriminating power
$\tau_e$	CMB-S4	0.047	0.033	$7\sigma$ with $\sigma(\tau_e) = 0.002$
$\langle f_{\text{esc}} \rangle$ at $z = 10$	JWST/NIRSpec	7%	4%	Direct LyC proxy via Ly $\alpha$ offsets
$f_{\text{esc}}$ at $M_h = 10^{9.5} M_\odot$ , $z = 11$	JWST	10–20%	$\sim 5\%$	Low-ionisation absorption lines
$\bar{x}_{\text{HI}}(z = 7)$	Ly $\alpha$ forest	0.30	0.13	Existing data favour steep model
$b_\gamma$ (emissivity-weighted bias)	SKA1-Low	4.75	4.75	$\sigma(\alpha_M) = 0.19$ ; breaks $\alpha_M$ - $\alpha_z$ degeneracy
Sub-threshold budget at $z = 10$	Ultra-deep JWST	$> 80\%$	$\sim 50\%$	Resolved by $M_{\text{UV}} \sim -14$ imaging

NOTE—Steep and flat predictions evaluated at the profile best-fit  $f_0$  and  $\alpha_M$ . The strongest discriminant is  $\tau_e$  from CMB-S4; JWST spectroscopy at  $z > 10$  provides the most direct test of  $f_{\text{esc}}$  evolution.

*SKA and 21 cm topology.* As shown in Section 8, SKA1-Low will constrain  $\sigma(\alpha_M) \sim 0.19$  in a moderate noise scenario, sufficient to distinguish  $\alpha_M = 0$  from  $\alpha_M = -0.25$ . Combined with our reionization-based  $\alpha_z$  constraint, this would provide the first complete empirical characterisation of  $f_{\text{esc}}(M_h, z)$  across both dimensions.

JWST Cycle 3–4 spectroscopic surveys will extend  $\xi_{\text{ion}}$  measurements to  $z > 10$  with reduced uncertainties, breaking the  $\xi_{\text{ion}}$ - $f_{\text{esc}}$  degeneracy that currently limits our  $f_0$  constraint. Ultra-deep imaging programs reaching  $M_{\text{UV}} \sim -14$  at  $z = 9$  will test the Schechter extrapolation and directly constrain the faint-end emissivity.

## 9. CONCLUSIONS

We have presented empirical constraints on a parametric mass-dependent escape fraction model  $f_{\text{esc}}(M_h, z)$  across the epoch of reionization. Our main findings are:

- 1. Mass dependence is unconstrained:** the marginal posterior gives  $\alpha_M = -0.52_{-0.69}^{+0.69}$ , spanning both mass-independent escape and the negative slopes predicted by simulations. The profile constraint ( $\alpha_M = 0.18 \pm 0.26$ ) is tighter but conditional on the other parameters. The reionization observables ( $\tau_e$ ,  $\bar{x}_{\text{HI}}(z)$ ) alone cannot determine whether low-mass or high-mass halos have higher  $f_{\text{esc}}$ .
- 2. Redshift evolution is steep in the profile likelihood:**  $\alpha_z = 1.98_{-0.42}^{+0.48}$  (profile), with  $\alpha_z > 1.0$  at  $> 99\%$  confidence. The marginal posterior ( $\alpha_z = 1.93_{-2.00}^{+2.09}$ ) is broader due to the  $f_0$ - $\alpha_M$  degeneracy but still favours  $\alpha_z > 0$  at 97% confidence.
- 3. Comparison with THESAN:** Fitting power laws directly to the THESAN-1 public escape frac-

tion catalogues, we find the luminosity-weighted mean has  $\alpha_z = 0.13$ , yielding  $\Delta\chi^2 = 13$  relative to our profile best fit. This represents moderate tension at the  $\sim 2\sigma$  level. Notably, the per-halo median in THESAN shows  $\alpha_z = 1.78$ , close to our profile value, but luminosity weighting suppresses this evolution. Breaking the parameter degeneracy with 21 cm topology, direct  $f_{\text{esc}}$  measurements, or mean-free-path constraints will clarify whether the steep profile preference is physical.

- 4. Sub-threshold halos dominate at high  $z$ :** At  $z \geq 10$ , halos below the UVLF detection threshold ( $M_h < 10^{10} M_\odot$ ) contribute more than 80% of the ionizing budget.
- 5. The population-averaged  $\langle f_{\text{esc}} \rangle(z)$  rises from  $\sim 2\%$  at  $z = 5$  to  $\sim 9\%$  at  $z = 12$ ,** lying below selected direct LyC samples at  $z < 4$ , as expected if those samples preferentially target high- $f_{\text{esc}}$  galaxies (Section 7.7).

These constraints provide the first data-driven calibration targets for reionization simulations. The tabulated  $f_{\text{esc}}(M_h, z)$  posteriors are provided in the online supplementary table for use as empirical inputs in semi-numerical and full RHD codes.

## 10. DATA AVAILABILITY

The code and data underlying this article are available at <https://github.com/wzh800557-source/fesc2d>. This includes the reionization solver, likelihood code, MCMC scripts, and a machine-readable table of  $f_{\text{esc}}(M_h, z)$  posteriors at 8 halo masses and 8 redshifts. The THESAN simulation data are available at <https://www.thesan-project.com/thesan/data.html>.

- 1 We acknowledge the support from NSFC of China under
- 2 grant 12533008

## REFERENCES

- Aghanim, N., et al. 2020, *Astron. Astrophys.*, 641, A6, doi: [10.1051/0004-6361/201833910](https://doi.org/10.1051/0004-6361/201833910)
- Ahn, K. 2021, *Bulletin of Korean Astronomical Society*, 46, 47.1
- Atek, H., Labbé, I., Furtak, L. J., et al. 2024, *nat*, 626, 975, doi: [10.1038/s41586-024-07043-6](https://doi.org/10.1038/s41586-024-07043-6)
- Becker, G. D., D'Aloisio, A., Christenson, H. M., et al. 2021, *Mon. Not. Roy. Astron. Soc.*, 508, 1853, doi: [10.1093/mnras/stab2696](https://doi.org/10.1093/mnras/stab2696)
- Begley, R., McLure, R. J., Cullen, F., et al. 2025, *MNRAS*, 537, 3245, doi: [10.1093/mnras/staf211](https://doi.org/10.1093/mnras/staf211)
- Behroozi, P., Wechsler, R. H., Hearin, A. P., & Conroy, C. 2019, *MNRAS*, 488, 3143, doi: [10.1093/mnras/stz1182](https://doi.org/10.1093/mnras/stz1182)
- Bolton, J. S., & Haehnelt, M. G. 2007, *Mon. Not. Roy. Astron. Soc.*, 382, 325, doi: [10.1111/j.1365-2966.2007.12372.x](https://doi.org/10.1111/j.1365-2966.2007.12372.x)
- Bosman, S. E. I., et al. 2022, *Mon. Not. Roy. Astron. Soc.*, 514, 55, doi: [10.1093/mnras/stac1046](https://doi.org/10.1093/mnras/stac1046)
- Bouwens, R. J., Oesch, P. A., Stefanon, M., et al. 2021, *aj*, 162, 47, doi: [10.3847/1538-3881/abf83e](https://doi.org/10.3847/1538-3881/abf83e)
- Bowler, R. A. A., Jarvis, M. J., Dunlop, J. S., et al. 2020, *Mon. Not. Roy. Astron. Soc.*, 493, 2059, doi: [10.1093/mnras/staa313](https://doi.org/10.1093/mnras/staa313)
- Carniani, S., Hainline, K., D'Eugenio, F., et al. 2024, *Nature*, 633, 318, doi: [10.1038/s41586-024-07860-9](https://doi.org/10.1038/s41586-024-07860-9)
- Dayal, P., & Ferrara, A. 2018, *Phys. Rept.*, 780-782, 1, doi: [10.1016/j.physrep.2018.10.002](https://doi.org/10.1016/j.physrep.2018.10.002)
- Donnan, C. T., McLure, R. J., Dunlop, J. S., et al. 2024, *MNRAS*, 533, 3222, doi: [10.1093/mnras/stae2037](https://doi.org/10.1093/mnras/stae2037)
- Eisenstein, D. J., & Hu, W. 1998, *Astrophys. J.*, 496, 605, doi: [10.1086/305424](https://doi.org/10.1086/305424)
- Endsley, R., Stark, D. P., Whitler, L., et al. 2024, *MNRAS*, 533, 1111, doi: [10.1093/mnras/stae1857](https://doi.org/10.1093/mnras/stae1857)
- Fan, X., Narayanan, V. K., Strauss, M. A., et al. 2002, *Astron. J.*, 123, 1247, doi: [10.1086/339030](https://doi.org/10.1086/339030)
- Finkelstein, S. L., D'Aloisio, A., Paardekooper, J.-P., et al. 2019, *Astrophys. J.*, 879, 36, doi: [10.3847/1538-4357/ab1ea8](https://doi.org/10.3847/1538-4357/ab1ea8)
- Finlator, K., Oh, S. P., Özel, F., & Davé, R. 2012, *MNRAS*, 427, 2464, doi: [10.1111/j.1365-2966.2012.22114.x](https://doi.org/10.1111/j.1365-2966.2012.22114.x)
- Furlanetto, S. R., Zaldarriaga, M., & Hernquist, L. 2004, *ApJ*, 613, 1, doi: [10.1086/423025](https://doi.org/10.1086/423025)
- Garaldi, E., et al. 2024, *Mon. Not. Roy. Astron. Soc.*, 530, 3765, doi: [10.1093/mnras/stae839](https://doi.org/10.1093/mnras/stae839)
- Greig, B., & Mesinger, A. 2017, *Mon. Not. Roy. Astron. Soc.*, 472, 2651, doi: [10.1093/mnras/stx2118](https://doi.org/10.1093/mnras/stx2118)
- Harikane, Y., Inoue, A. K., Ellis, R. S., et al. 2025, *ApJ*, 980, 138, doi: [10.3847/1538-4357/ad9b2c](https://doi.org/10.3847/1538-4357/ad9b2c)
- Izotov, Y. I., Worseck, G., Schaerer, D., et al. 2018, *MNRAS*, 478, 4851, doi: [10.1093/mnras/sty1378](https://doi.org/10.1093/mnras/sty1378)
- Kannan, R., Garaldi, E., Smith, A., et al. 2022, *MNRAS*, 511, 4005, doi: [10.1093/mnras/stab3710](https://doi.org/10.1093/mnras/stab3710)
- Kimm, T., & Cen, R. 2014, *ApJ*, 788, 121, doi: [10.1088/0004-637X/788/2/121](https://doi.org/10.1088/0004-637X/788/2/121)
- Koopmans, L. V. E., et al. 2015, *PoS, AASKA14*, 001, doi: [10.22323/1.215.0001](https://doi.org/10.22323/1.215.0001)
- Llerena, M., Pentericci, L., Napolitano, L., et al. 2025, *Astronomy and Astrophysics*, 698, A302, doi: [10.1051/0004-6361/202453251](https://doi.org/10.1051/0004-6361/202453251)
- Ma, X., Quataert, E., Wetzel, A., et al. 2020, *Mon. Not. Roy. Astron. Soc.*, 498, 2001, doi: [10.1093/mnras/staa2404](https://doi.org/10.1093/mnras/staa2404)
- Madau, P., Haardt, F., & Rees, M. J. 1999, *Astrophys. J.*, 514, 648, doi: [10.1086/306975](https://doi.org/10.1086/306975)
- Mascia, S., Pentericci, L., Calabrò, A., et al. 2023, *Astronomy and Astrophysics*, 672, A155, doi: [10.1051/0004-6361/202345866](https://doi.org/10.1051/0004-6361/202345866)
- Mason, C., Trenti, M., & Treu, T. 2015, *Astrophys. J.*, 813, 21, doi: [10.1088/0004-637X/813/1/21](https://doi.org/10.1088/0004-637X/813/1/21)
- Mason, C. A., et al. 2019, *Mon. Not. Roy. Astron. Soc.*, 485, 3947, doi: [10.1093/mnras/stz632](https://doi.org/10.1093/mnras/stz632)
- McGreer, I., Mesinger, A., & D'Odorico, V. 2015, *Mon. Not. Roy. Astron. Soc.*, 447, 499, doi: [10.1093/mnras/stu2449](https://doi.org/10.1093/mnras/stu2449)
- McQuinn, M., Lidz, A., Zahn, O., et al. 2007, *Mon. Not. Roy. Astron. Soc.*, 377, 1043, doi: [10.1111/j.1365-2966.2007.11489.x](https://doi.org/10.1111/j.1365-2966.2007.11489.x)
- Naidu, R. P., Tacchella, S., Mason, C. A., et al. 2019, doi: [10.3847/1538-4357/ab7cc9](https://doi.org/10.3847/1538-4357/ab7cc9)
- Ono, Y., Harikane, Y., Ouchi, M., et al. 2023, *apj*, 951, 72, doi: [10.3847/1538-4357/acd44a](https://doi.org/10.3847/1538-4357/acd44a)
- Paardekooper, J.-P., Khochfar, S., & Vecchia, C. D. 2015, *Mon. Not. Roy. Astron. Soc.*, 451, 2544, doi: [10.1093/mnras/stv1114](https://doi.org/10.1093/mnras/stv1114)
- Pahl, A. J., Topping, M. W., Shapley, A., et al. 2025, *Astrophys. J.*, 981, 134, doi: [10.3847/1538-4357/adb1ab](https://doi.org/10.3847/1538-4357/adb1ab)
- Robertson, B. E., Ellis, R. S., Furlanetto, S. R., & Dunlop, J. S. 2015, *ApJL*, 802, L19, doi: [10.1088/2041-8205/802/2/L19](https://doi.org/10.1088/2041-8205/802/2/L19)
- Rosdahl, J., Blaizot, J., Katz, H., et al. 2022, *MNRAS*, 515, 2386, doi: [10.1093/mnras/stac1942](https://doi.org/10.1093/mnras/stac1942)
- Sheth, R. K., & Tormen, G. 1999, *Mon. Not. Roy. Astron. Soc.*, 308, 119, doi: [10.1046/j.1365-8711.1999.02692.x](https://doi.org/10.1046/j.1365-8711.1999.02692.x)
- Shull, J. M., Harness, A., Trenti, M., & Smith, B. D. 2012, *ApJ*, 747, 100, doi: [10.1088/0004-637X/747/2/100](https://doi.org/10.1088/0004-637X/747/2/100)
- Simmonds, C., Tacchella, S., Maseda, M., et al. 2023, *MNRAS*, 523, 5468, doi: [10.1093/mnras/stad1749](https://doi.org/10.1093/mnras/stad1749)

- Steidel, C. C., Bogosavljevic, M., Shapley, A. E., et al. 2018, *Astrophys. J.*, 869, 123, doi: [10.3847/1538-4357/aaed28](https://doi.org/10.3847/1538-4357/aaed28)
- Tang, M., Stark, D. P., Chen, Z., et al. 2023, *MNRAS*, 526, 1657, doi: [10.1093/mnras/stad2763](https://doi.org/10.1093/mnras/stad2763)
- Tinker, J. L., Kravtsov, A. V., Klypin, A., et al. 2008, *Astrophys. J.*, 688, 709, doi: [10.1086/591439](https://doi.org/10.1086/591439)
- Trebitsch, M., Blaizot, J., Rosdahl, J., Devriendt, J., & Slyz, A. 2017, *MNRAS*, 470, 224, doi: [10.1093/mnras/stx1060](https://doi.org/10.1093/mnras/stx1060)
- Umeda, H., Ouchi, M., Nakajima, K., et al. 2024, *ApJ*, 971, 124, doi: [10.3847/1538-4357/ad554e](https://doi.org/10.3847/1538-4357/ad554e)
- Wang, Z. 2026. <https://arxiv.org/abs/2604.10726>
- Wang, Z., & Shan, H. 2026. <https://arxiv.org/abs/2605.03635>
- Ward, E., de la Vega, A., Mobasher, B., et al. 2024, *apj*, 962, 176, doi: [10.3847/1538-4357/ad20ed](https://doi.org/10.3847/1538-4357/ad20ed)
- Xu, H., Wise, J. H., Norman, M. L., Ahn, K., & O’Shea, B. W. 2016, *apj*, 833, 84, doi: [10.3847/1538-4357/833/1/84](https://doi.org/10.3847/1538-4357/833/1/84)
- Yeh, J. Y. C., Smith, A., Kannan, R., et al. 2023, *Mon. Not. Roy. Astron. Soc.*, 520, 2757, doi: [10.1093/mnras/stad210](https://doi.org/10.1093/mnras/stad210)
- Zhu, Y., Becker, G. D., Bosman, S. E. I., et al. 2023, *ApJ*, 955, 115, doi: [10.3847/1538-4357/aceef4](https://doi.org/10.3847/1538-4357/aceef4)